Ray-Tracing and Physical-Optics Model for Planar Mikaelian Lens Antennas

Mingzheng Chen, *Student Member, IEEE,* Ozum Habiboglu, Francisco Mesa, *Fellow, IEEE,* and Oscar Quevedo-Teruel, *Fellow, IEEE*

***Abstract*—This article proposes a ray-tracing and physical-optics (RT-PO) model that allows for an accurate and time-efficient evaluation of planar Mikaelian lens antennas implemented by parallel plate waveguides. With an intrinsic flat shape and axis-symmetry of refractive-index distribution characteristic, the planar Mikaelian lens antennas are easy to fabricate and integrate to standard planar feeds. A numerical computation of the ray paths based on the Snell's law gives a description of the phase of the electric field in the lens aperture, while the ray-tube power conservation theory is employed to evaluate the amplitude. The field equivalence principle is then used to calculate the far field of the lens antenna. The information of far-field directivity, gain, and dielectric efficiency is further obtained, considering a small loss in the dielectric materials. Our approach is validated by comparing the results of a particular Mikaelian lens antenna with those computed using a commercial full-wave simulator, demonstrating high accuracy and significant reduction in computation resources and times.**

***Index Terms*—Dielectric efficiency, directivity, gain, Mikaelian lens antenna, parallel plate waveguide, physical optics, ray tracing.**

I. Introduction

NOWADAYS, our modern society is experiencing a growing need for high-speed wireless communications to meet the demands of emerging mobile applications, such as cloud-based virtual reality, autonomous driving, wireless medical services, etc. The limited availability of spectrum in the lower frequency bands, often referred to as sub-6 GHz, makes it difficult to meet these high capacity demands. In recent years, there has been a surge in research on higher frequency bands, particularly millimeter waves and beyond, to take advantage of the plentiful spectrum resources available [1], [2]. At such high frequencies, beamforming devices are essential to generate high-gain antenna solutions to compensate for the considerable path losses while still maintaining the large coverage with beam-steering or multiple-beam capabilities. However, conventional microwave components and antennas, such as beamforming networks and printed circuit board phased arrays, are expensive for mass production. Consequently, quasi-optical solutions are generally the preferred choice for highly directive and cost-effective multiple-beam antennas at high frequencies, as they are simpler to construct and more tolerant of manufacturing mistakes [3]–[5]. Well-known solutions include reflector-based antennas [6], [7], homogeneous dielectric lens antennas [8]–[10], gradient index (GRIN) dielectric lens antennas [11], [12], and parallel plate lens antennas [13], [14].

Compared to homogeneous lenses, GRIN lenses are generally more flexible in achieving large beam-steering angles with competitive efficiencies and broad operating bands. There have been several renowned GRIN lens antennas, such as the Luneburg lens antenna [15], the half-Maxwell fish-eye lens antenna [16], [17], and the Gutman lens antenna [18], [19]. Despite the fact that all of the GRIN lenses mentioned have graded refractive-index distributions, they all share the same feature of having a curved feeding interface, making it difficult to integrate them into standard planar feeds. To overcome this limitation, transformation optics, and in particular the quasi-conformal transformation optics method, were proposed to modify the shape of the lens and the corresponding refractive-index distributions [20]–[23]. However, these conformal mapping transformations typically cause a reduction in beam-steering capabilities and an increase in the complexity of implementation. Unlike these spherically symmetric lenses, the Mikaelian lens, also called the hyperbolic cosine lens, has a unique flat shape characteristic of both the feeding interface and the lens aperture [24], [25]. Moreover, the Mikaelian lens can be easily fabricated due to the intrinsic cylindrical symmetry of its refractive-index distribution. As a result, it has recently attracted a great deal of attention in the applications of microwave and millimeter-wave components and antennas [26]–[31].

For applications requiring only one-axis beam scanning, a planar (two-dimensional, 2-D) version of the aforementioned lenses can be implemented in a parallel plate waveguide (PPW) configuration [32]–[36]. Full-wave simulators are typically used to study the wave propagation and far-field radiation characteristics of the PPW lenses. However, as the electrical size of the lenses increases, these full-wave simulations require considerably long computation times and high memory resources, which hinders the design of PPW lenses through optimization because of the time limitations. Consequently, ray-tracing (RT) tools based on geometrical optics (GO) have been found to be both precise and time-efficient [37]–[43].

The work of O. Quevedo-Teruel was funded by the VR Project (2022-03865) under the call "Research project grant within natural and engineering sciences".

The work of F. Mesa has been partially supported by the PID2020-116739GB-I00 grant funded by MCIN/AEI/10.13039/501100011033.

M. Chen, O. Habiboglu, and O. Quevedo-Teruel are with the Division of Electromagnetic Engineering and Fusion Science, KTH Royal Institute of Technology, SE-100 44 Stockholm, Sweden (e-mails: mzchen@kth.se; ozum@kth.se; oscarqt@kth.se).

F. Mesa is with the Department of Applied Physics 1, ETS Ingeniería Informática, Universidad de Sevilla, 41012, Spain (e-mail: mesa@us.es).

Manuscript received Month XX, 202X; revised Month XX, 202X. *(Corresponding author: O. Quevedo-Teruel.)*

Although the RT tool proposed in those papers is capable of giving a good description of the wavefront of electromagnetic waves confined inside the PPW, this approach is restricted to the analysis of the radiation patterns in the beamforming plane (the H-plane) of PPW lenses. In other words, compared to commercial simulators, relevant information is missing, including the full radiation pattern, directivity, gain, and dielectric efficiency.

In this article, we propose an RT and Physical-Optics (PO) model, named the RT-PO model, to obtain the radiation pattern, directivity, gain, and dielectric efficiency of planar Mikaelian lens antennas. The implementation of the PO approximation combined with the RT approach is demonstrated to be considerably accurate and highly time-efficient when comparing the obtained results to well-established commercial full-wave simulators.

The article is organized as follows. In Section II, we propose an RT-PO model to analyze planar Mikaelian lens antennas, taking into account the unique properties of the lens. In Section III, detailed numerical results of the implementation of the method in a particular Mikaelian lens antenna are presented and discussed. The accuracy and computational efficiency of the algorithm is also evaluated by comparing it with a commercial full-wave simulator. Finally, some conclusions are drawn in Section IV.

II. Ray-Tracing and Physical-Optics Model

A. Ray Tracing for Mikaelian Lenses

First proposed by A. L. Mikaelian [24], Mikaelian lenses are capable of transforming rays excited from one point in a flat feeding interface to collimated rays in a flat aperture. In this article, we focus on planar Mikaelian lens antennas realized with GRIN dielectric materials within PPWs, as illustrated in Fig. 1(a), where L denotes the length of the lens along the z-axis and R half the width along the x-axis. Under this coordinate system (x, z), the refractive-index profile is defined as follows:

$$n(x) = \frac{n_0}{\cosh\left(\dfrac{\pi|x|}{2L}\right)} \tag{1}$$

where n_0 is the refractive index when $x = 0$ and the profile is constant in the z-direction. The propagation of waves in this planar Mikaelian lens antenna takes the form of a transverse electromagnetic (TEM) mode assuming that the height of the PPW, h, is small enough compared to the operating wavelength. To avoid exciting high-order TE/TM modes, the operating frequency should be lower than $c/2hn_0$, where c is the speed of light in vacuum. Furthermore, Fig. 1(b) depicts the corresponding model of the Mikaelian lens antenna used in the full-wave simulator, including the rectangular waveguide feed and the flare structure; the details will be discussed in Section III. As stated in Section I, the analysis of wave propagation and the resulting radiation characteristics of PPW beamformers is generally performed with commercial full-wave simulators [36]. These simulators require a lot of computing power and time, so RT-based techniques combined with PO procedures have been developed to be more accurate and faster [37]–[44]. However, existing methods are restricted to the analysis of two-dimensional (2-D) radiation patterns in the beamforming plane. In this paper, we present an RT model based on Snell's law to calculate the electric field in the opening of the planar Mikaelian lens, along with a straightforward implementation of the field equivalence principle for computing full three-dimensional (3-D) radiation patterns in every direction. Thus, we can also calculate directivity, gain, dielectric loss, and radiation efficiency from our proposed RT-PO model.

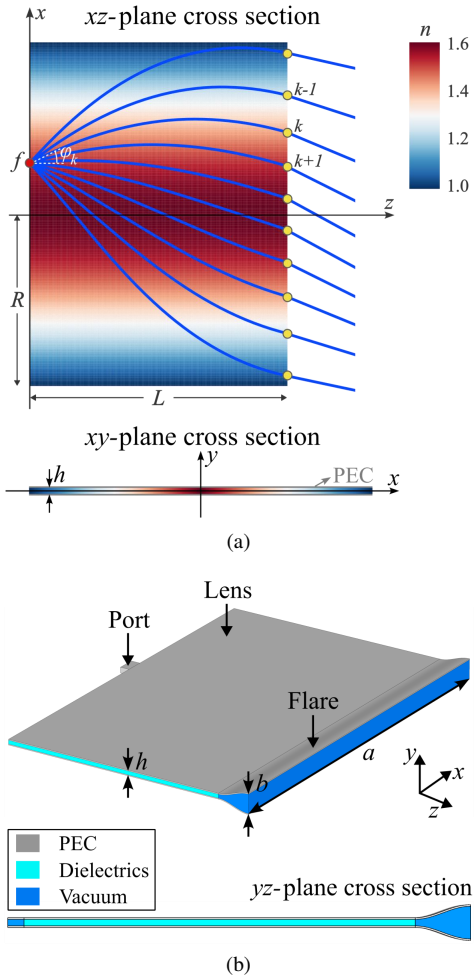

Fig. 1. (a) Illustration of ray tracing inside a planar Mikaelian lens antenna and the cross section in the xy-plane. (b) Full-wave (CST) model of a planar Mikaelian lens antenna and the cross section in the yz-plane, including the feed port, lens, and radiation flare structure.

In the GO approximation, rays are defined as trajectories perpendicular to the wavefronts of the electromagnetic (EM) waves [45]–[47]. To be effective and precise, the GO approach must meet two conditions: (i) the lens size must be sufficiently large compared to the wavelength λ, and (ii) the refractive index should vary smoothly per wavelength. This second condition also implies that reflections can be disregarded in the direction of the changing refractive index. As illustrated in Fig. 1(a), in our RT model, a family of rays are traced from the source point f (colored red) to the target points (colored yellow) in the aperture, with the k-th ray having a starting departure angle φ_k. The refractive index of the

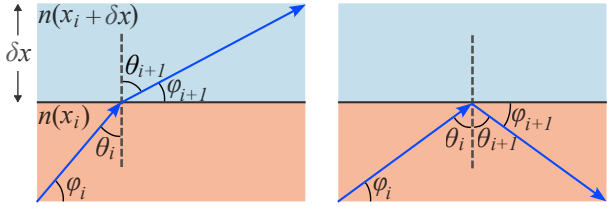

Fig. 2. Interface between two dielectric materials of thickness δx, where $n(x_i+\delta x) < n(x_i)$. (a) A ray is transmitted from the lower layer to the upper layer when $\theta_i < \theta_c$. (b) A ray reflects at the interface when $\theta_i \geq \theta_c$.

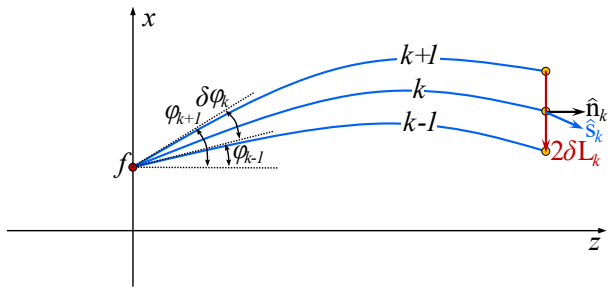

Fig. 3. Illustration of the k-th ray tube to evaluate the E-field amplitude in the lens aperture.

Mikaelian lens changes only in the vertical direction along the x-axis, as indicated in (1). To account for this, we divide the inhomogeneous dielectric material in the x-direction into N homogeneous layers with a thickness of δx ($\delta x = 2R/N$), where the variation of the dielectric material between layers is minimal. Figure 2 depicts the behavior of a ray at any inner interface between two dielectric materials located at positions x_i and $x_i + \delta x$, respectively, with i denoting the i-th segment S_i of the ray. Here, we assume that $x_i > 0$ and hence $n(x_i) > n(x_i + \delta x)$ [other scenarios have been omitted for the sake of brevity without losing generality]. For the i-th segment S_i, the departure angle φ_i is known; therefore, the incident angle θ_i is equal to $(\pi/2 - \varphi_i)$. When θ_i is smaller than the critical angle θ_c, which is equal to $\arcsin[n(x_i+\delta x)/n(x_i)]$, the ray transits from the lower layer to the upper layer, and the refractive angle θ_{i+1} is equal to $\arcsin[n(x_i)\sin\theta_i/n(x_i + \delta x)]$, as shown in Fig. 2(a). Otherwise, the ray completely reflects at the interface with a reflection angle $\theta_{i+1} = \theta_i$, as plotted in Fig. 2(b). In both cases, the departure angle φ_{i+1} is obtained using $\varphi_{i+1} = \pi/2 - \theta_{i+1}$ and the $(i+1)$-th segment S_{i+1} is traced accordingly. As a result, with a known position of the source point f and predefined starting departure angles φ_k, all rays can be traced.

B. Electric Field in the Lens Aperture

In this subsection, the electric field in the lens aperture, including both amplitude and phase, is obtained using the information provided by the traced rays. First, the amplitude A_k at each target point k of the lens aperture is computed using the ray-tube power conservation theory [37], [40], [45], [47]. Following the notation in Fig. 3, this amplitude is given by the following equation:

$$A_k = A'_k \sqrt{\frac{\delta\varphi_k}{\delta L_k(\hat{\mathbf{s}}_k \cdot \hat{\mathbf{n}}_k)}} \tag{2}$$

where A'_k is the amplitude at a reference position near the feed, $\delta\varphi_k = (\varphi_{k+1} - \varphi_{k-1})/2$ is the subtended angle of the k-th ray tube at the source position, $\delta L_k = (x_{k+1} - x_{k-1})/2$ is the width of the k-th ray tube in the aperture, $\hat{\mathbf{n}}_k$ is the unit vector normal to the lens aperture, and $\hat{\mathbf{s}}_k$ is the unit vector along the direction of the k-th ray outside the lens aperture, corresponding to the local Poynting vector. The feed amplitude A'_k depends only on the source excitation, provided that the PPW has a constant height h. Typically, the directive open-ended waveguide is used to feed PPW lenses. Here, we approximate the amplitude distribution of the feed waveguide by a Gaussian function defined as

$$A'_k = 10^{-(3\zeta^2/20)} \tag{3}$$

where $\zeta = \varphi_k/\varphi_{3\mathrm{dB}}$ is the ratio between the angle of departure, φ_k, and the half-power beamwidth angle, $\varphi_{3\mathrm{dB}}$, the same as in [37].

Phase Φ_k and dielectric loss ξ_k associated with the electric field at the target point k in the aperture are obtained by adding phase variation Φ_i and dielectric loss ξ_i in all segments of the k-th ray. Assuming that the dielectric material for the i-th segment of the k-th ray has a complex relative dielectric permittivity $\epsilon_{ri} = \epsilon'_{ri} + \mathrm{j}\epsilon''_{ri}$ with a small dielectric loss ($\epsilon''_{ri} \ll \epsilon'_{ri}$) [as usually found in dielectric lenses], the complex wavenumber of the material is given by

$$k_i = \beta_i - \mathrm{j}\alpha_i \tag{4}$$

with

$$\beta_i \approx \sqrt{\epsilon'_{ri}} k_0 = n_i k_0 \tag{5}$$

$$\alpha_i \approx \frac{\beta_i}{2}\left(\frac{\epsilon''_{ri}}{\epsilon'_{ri}}\right) = \frac{\beta_i}{2}\tan\delta \tag{6}$$

where k_0 is the wavenumber in the free space, n_i the refractive index, and $\tan\delta$ the dielectric loss factor. Given that the length of the i-th segment is $\sigma_i = \delta x/\sin\varphi_i$, the phase variation Φ_i and dielectric loss ξ_i in the i-th segment of the k-th ray are

$$\Phi_i = \beta_i \sigma_i \tag{7}$$

$$\xi_i = \alpha_i \sigma_i \tag{8}$$

and, therefore, the phase Φ_k and dielectric loss ξ_k associated with the k-th ray are calculated as

$$\Phi_k = \sum_i \Phi_i = \sum_i n_i k_0 \sigma_i \tag{9}$$

$$\xi_k = \sum_i \xi_i = \sum_i \left(\frac{n_i k_0}{2}\tan\delta\right)\sigma_i\ . \tag{10}$$

Knowing the amplitude, phase, and dielectric loss, the E-field distribution in the lens aperture is finally obtained as

$$\mathbf{E}_k = A_k \mathrm{e}^{-\mathrm{j}\Phi_k}\mathrm{e}^{-\xi_k}\hat{\mathbf{y}}. \tag{11}$$

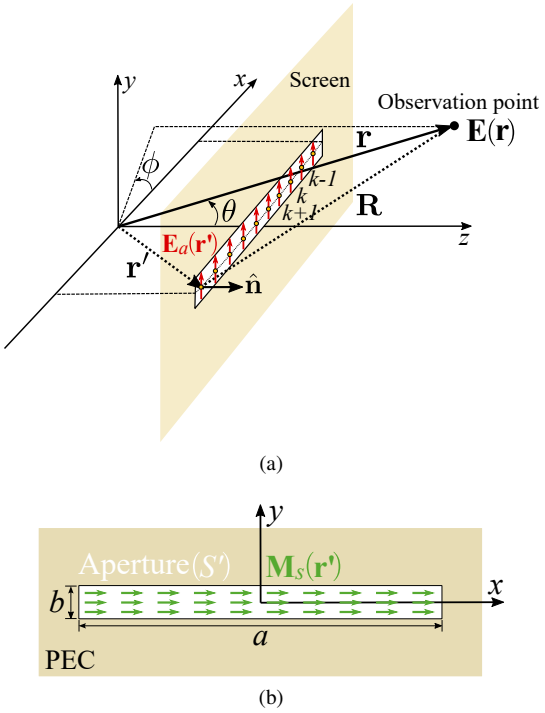

Fig. 4. (a) Geometric parameters and coordinate system for numerical evaluation of the 3-D radiation characteristics. (b) Aperture distribution of the equivalent magnetic current assuming the screen around the aperture is PEC.

C. 3-D Far-Zone Electric Fields

In this work, the 3-D radiation characteristics of the planar Mikaelian lens antennas are evaluated using a simplified implementation of the PO approximation (i.e., the field equivalence principle) [48]. This approach is based on sensible estimates of the fields on and in the vicinity of the antenna aperture, which are particularly suitable for PPW lens antennas. As illustrated in Fig. 4(a), we model the Mikaelian lens antenna as a thin aperture surrounded by an infinite screen, with an aperture electric field denoted as $\mathbf{E}_a(\mathbf{r}')$ and $\mathbf{r}'$ being any point in the lens aperture. Under a reasonable assumption that the infinite screen is a perfect electric conductor (PEC), the actual source $\mathbf{E}_a(\mathbf{r}')$ is replaced by the following equivalent magnetic source:

$$\mathbf{M}_s(\mathbf{r}') = -2\hat{\mathbf{n}} \times \mathbf{E}_a(\mathbf{r}') \tag{12}$$

where $\hat{\mathbf{n}}$ is the unit vector normal to the aperture. As the lens aperture is located in the xy plane, $\mathbf{M}_s(\mathbf{r}') = 2E_a(x')\hat{\mathbf{x}}$, as plotted in Fig. 4(b), assuming that the lens works in the fundamental TEM mode. As a result, the far-field expression of the electric field produced by the equivalent magnetic source in the lens aperture (S') is given by [48], [49]

$$\mathbf{E} = -\mathrm{j}k_0 \frac{\mathrm{e}^{-\mathrm{j}k_0 r}}{4\pi r} \hat{\mathbf{r}} \times [-\widetilde{\mathbf{L}}] \tag{13}$$

where $\widetilde{\mathbf{L}}$ stands for

$$\widetilde{\mathbf{L}}(\theta,\phi) = \widetilde{L}_\theta \hat{\boldsymbol{\theta}} + \widetilde{L}_\phi \hat{\boldsymbol{\phi}} = \int_S \mathbf{M}_s(\mathbf{r}') \mathrm{e}^{\mathrm{j}\mathbf{k}_0 \cdot \mathbf{r}'} \mathrm{d}S' \tag{14}$$

in which $\mathbf{k}_0 = k_0\hat{\mathbf{r}} = k_x\hat{\mathbf{x}} + k_y\hat{\mathbf{y}} + k_z\hat{\mathbf{z}}$ is a wavevector with components $k_x = k_0 \cos\phi \sin\theta$, $k_y = k_0 \sin\phi \sin\theta$ and $k_z = k_0 \cos\theta$. Introducing (14) into (13), the far-zone electric field can be written in spherical coordinates as

$$\mathbf{E}(r,\theta,\phi) = E_\theta\hat{\boldsymbol{\theta}} + E_\phi\hat{\boldsymbol{\phi}} = -\mathrm{j}k_0 \frac{\mathrm{e}^{-\mathrm{j}k_0 r}}{4\pi r}(\widetilde{L}_\phi\hat{\boldsymbol{\theta}} - \widetilde{L}_\theta\hat{\boldsymbol{\phi}}) \ . \tag{15}$$

Combining the equations (11)-(15) together, the far-zone E-field radiated by the lens aperture can be finally computed with (29) and (30), which are given in Appendix A.

With this information, we can calculate the radiation patterns in the E- and H-planes. According to the coordinate definition in Fig. 4(a), the E-plane pattern is in the yz-plane ($\phi = \pi/2$), and the far-zone E-field is

$$E_r = 0 = E_\phi \tag{16}$$

$$E_\theta(\theta) = \mathrm{j}k_0 b \frac{\mathrm{e}^{-\mathrm{j}k_0 r}}{2\pi r} \frac{\sin(\frac{k_0 b}{2}\sin\theta)}{\frac{k_0 b}{2}\sin\theta} \sum_k A_k \mathrm{e}^{-\xi_k} \mathrm{e}^{-\mathrm{j}\Phi_k} \delta L_k \ . \tag{17}$$

Similarly, the far-zone H-plane E-field in the xz-plane ($\phi = 0$) is given by

$$E_r = E_\theta = 0 \tag{18}$$

$$E_\phi(\theta) = \mathrm{j}k_0 b \frac{\mathrm{e}^{-\mathrm{j}k_0 r}}{2\pi r} \sum_k A_k \mathrm{e}^{-\xi_k} \mathrm{e}^{-\mathrm{j}(\Phi_k - k_0 x_k \sin\theta)} \delta L_k \ . \tag{19}$$

It is worth emphasizing that the H-plane is the beamforming plane of the Mikaelian lens antenna, so more attention will be paid to this plane when studying the lens' beam-scanning characteristics.

D. Reflections and Virtual Source

In the preceding analysis, a simplification was assumed in that all the EM waves that reached the lens aperture would be transmitted directly to the open air; that is, the refraction between the lens and the open air was taken into account but not the reflections. However, because of the varying refractive-index distribution in the lens aperture, part of the waves will be reflected into the lens. The reflected waves in the aperture can be modeled as rays traced back inside the lens, and their amplitude will be given by the reflection coefficients following the Fresnel formulae.

As depicted in Fig. 5(a), a family of rays emitted from the actual source f (colored blue) arrive at the lens aperture. For a clearer illustration, only the rays with the departure angle $\varphi_k > 0$ are plotted in the figure. These rays will continue into free space. However, part of the EM waves will be reflected. Due to the self-focusing property of the Mikaelian lens, the corresponding reflected rays (colored green) converge to a virtual source f', which is symmetric to the primary source f with respect to the z-axis. At the interface $z = 0$, these rays are again partially reflected and transmitted. The transmitted rays are omitted in the figure and ignored in our analysis because they do not contribute to the forward radiation. The reflected rays, which are colored purple, can be seen as emitted from a virtual source f' and travel to the lens aperture where they radiate out in combination with the originally transmitted blue rays. A portion of the EM waves from the virtual source is again reflected/refracted in the aperture, resulting in multiple reflections and transmissions.

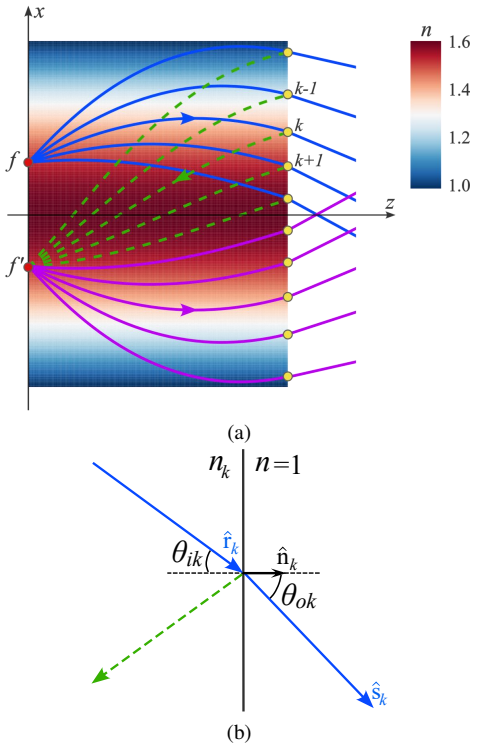

Fig. 5. (a) Illustration of ray tracing inside a planar Mikaelian lens antenna considering the effect of a virtual source f'. (b) Illustration of the k-th ray in the Mikaelian lens aperture to evaluate the transmission and reflection coefficient.

However, the effect of this is minimal and is not taken into account in our model. Furthermore, due to the symmetry property of the Mikaelian lens, we can observe in Fig. 5(a) that the purple rays from f' are z-axially symmetric with the blue rays from f, so they do not need to be calculated in the code, thus reducing computation time and memory resources.

In order to quantify the amount of reflected and transmitted EM waves associated with the k-th ray emitted from the primary source f, we make use of the reflection Fresnel coefficient [49], which can be expressed as

$$\rho_k = \frac{n_k(\hat{\mathbf{r}}_k \cdot \hat{\mathbf{n}}_k) - \hat{\mathbf{s}}_k \cdot \hat{\mathbf{n}}_k}{n_k(\hat{\mathbf{r}}_k \cdot \hat{\mathbf{n}}_k) + \hat{\mathbf{s}}_k \cdot \hat{\mathbf{n}}_k} \tag{20}$$

where $\hat{\mathbf{r}}_k$ and $\hat{\mathbf{s}}_k$ are the unit vectors associated to the incoming and outgoing directions of the rays, as shown in Fig. 5(b). From (20), the transmission Fresnel coefficient is calculated as $\tau_k = 1 + \rho_k$, that is,

$$\tau_k = \frac{2n_k(\hat{\mathbf{r}}_k \cdot \hat{\mathbf{n}}_k)}{n_k(\hat{\mathbf{r}}_k \cdot \hat{\mathbf{n}}_k) + \hat{\mathbf{s}}_k \cdot \hat{\mathbf{n}}_k} \,. \tag{21}$$

The magnitudes of the reflection and transmission power coefficients are then given by [49]

$$\mathscr{R}_k = |\rho_k|^2 \tag{22}$$

$$\mathscr{T}_k = |\tau_k|^2 \frac{\hat{\mathbf{s}}_k \cdot \hat{\mathbf{n}}_k}{|n_k|(\hat{\mathbf{r}}_k \cdot \hat{\mathbf{n}}_k)} \,. \tag{23}$$

Since the ray tracing provides the amplitude of the electric field through the power conservation of the ray tube [see Eq. (2)], the relevant coefficients for the field amplitude, here denoted as R_k and T_k, must be obtained from the power coefficients in (22) and (23) as

$$R_k = \sqrt{\mathscr{R}_k} = |\rho_k| \tag{24}$$

$$T_k = \sqrt{\mathscr{T}_k} = |\tau_k| \sqrt{\frac{\hat{\mathbf{s}}_k \cdot \hat{\mathbf{n}}_k}{|n_k|(\hat{\mathbf{r}}_k \cdot \hat{\mathbf{n}}_k)}} \,. \tag{25}$$

Due to the aforementioned symmetry properties of the Mikaelian lens, the calculation of the reflection coefficient R'_k associated with the k-th ray of the virtual source f' can be omitted since it is the same as R_k. It can also be clearly observed from Fig. 5(a) that the phase distribution for the purple rays is the reverse of that for the blue rays and that the dielectric loss is the same. However, the dielectric loss of the green rays must be calculated explicitly, and the process is the same as that of the blue rays with an angle of $-\varphi_k$.

Taking all of the above into account, we finally obtain the E-field associated with the k-th ray in the lens aperture as

$$E_k = A_k \mathrm{e}^{-\mathrm{j}\Phi_k} \mathrm{e}^{-\xi_k} T_k \left[1 + R_k R'_k \mathrm{e}^{\mathrm{j}2\Phi_k} \mathrm{e}^{-(\xi_k + \xi_k^{(-)})}\right] \tag{26}$$

where the first and second terms are the aperture fields associated with the primary and virtual sources, and $\xi_k^{(-)}$ denotes the dielectric loss of the ray with a departure angle $-\varphi_k$. Introducing (26) into the corresponding expressions for the far-zone E-field, we can now obtain the directivity $D(\theta, \phi)$ and gain $G(\theta, \phi)$ of the Mikaelian lens antenna applying (31) and (32) given in Appendix B. Subsequently, the corresponding dielectric efficiency e_d and the total radiation efficiency (including reflections) can be calculated.

It should be noted that all the information in (26) is provided by the blue rays that have been traced from the primary source f; thus, taking into account the effect of the virtual source does not add to the complexity of the proposed RT-PO model.

III. Numerical Results

To validate the proposed RT-PO approach for planar Mikaelian lens antennas, we consider a particular case with $R = 100\,\mathrm{mm}$, $L = 120\,\mathrm{mm}$, and $n_0 = 2$ (see Fig. 1). At the design frequency of 30 GHz, R and L correspond to 10λ and 12λ, respectively. In addition, we assume a small dielectric loss factor of $\tan\delta = 10^{-3}n(x)$. In this section, the height of the PPW is $h = 2\,\mathrm{mm}$ to ensure that only the fundamental mode is operating. The numerical results of the RT-PO model are validated by comparing them with the full-wave simulation results acquired with the CST software. This software has already been shown to be in close agreement with the experimental results of multiple PPW lens antennas [50]–[52].

A. Aperture Electric Field

First, we validate our RT procedure to calculate the E-field in the lens aperture, a computation that is key for a further accurate evaluation of the electric far fields. In particular, Fig. 6 shows the normalized amplitude and phase distributions of the E-field in the lens aperture ($z = L$) obtained from RT and CST at 30 GHz with the source f located at $x = 1\lambda$. Following (3),

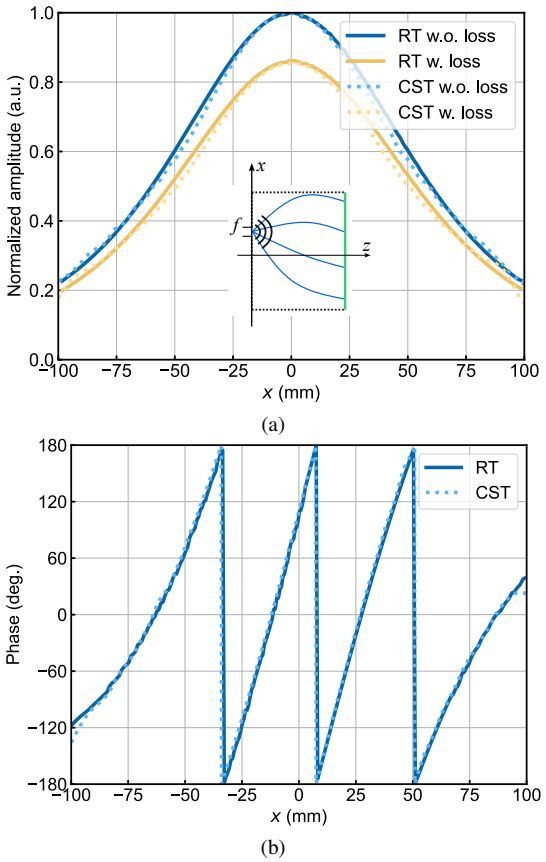

Fig. 6. (a) Normalized amplitude and (b) phase distributions of the E-field in the aperture of the lens obtained from RT and CST at 30 GHz with the source f located at $x = 1\lambda$ (inset: illustration of the Mikaelian lens fed by an open-ended waveguide with the width of 8.64 mm; lens aperture is in green).

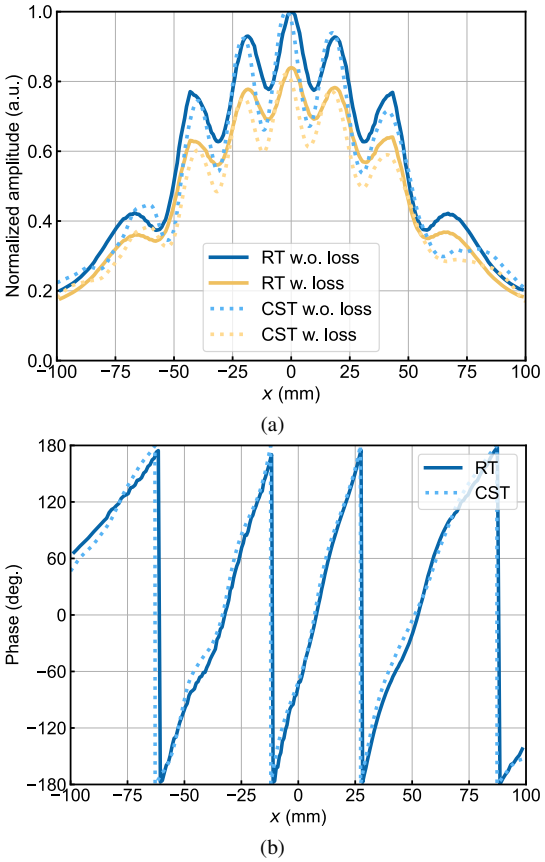

Fig. 7. (a) Normalized amplitude and (b) phase distributions of the E-field in the aperture of the lens obtained from RT and CST at 30 GHz with the source f located at $x = 1\lambda$, including the effect of the virtual source f'.

an open-ended waveguide feed is used as the source with the width of 8.64 mm, matching the dimensions of standard WR34 operating at the K_a-band; the height of the waveguide feed is the same as the PPW height h of 2 mm. The feed model is adjusted at 30 GHz with $\varphi_{3\text{dB}} = 32.5°$ and a phase center displacement of 0.1λ within the lens.

In our first analysis, the wave reflections in the lens aperture are omitted in the RT model [that is, $R_k = 0$ in (26)], and hence we set an open boundary condition (perfect matching layer) to eliminate the reflections in the lens aperture in the CST modeling. In this case, Fig. 6(a) shows that both the RT and CST amplitudes agree well with (w.) and without (w.o.) dielectric losses, thus validating our evaluation of the field amplitude by means of the ray-tube power, as well as our treatment of dielectric losses. It should be noted that the results with losses are slightly asymmetric with respect to $x = 0$, because the rays arriving at the opposite position in the aperture ($z = L$) pass through layers of material with different dielectric loss factors. In Fig. 6(b), it is also shown that the phase in the aperture obtained with RT agrees very well with the CST results, which confirms the operation of the proposed RT method and the accuracy of the phase of the traced rays.

If reflections in the aperture are now included in the RT model [$R_k \neq 0$ in (26)], the E-field in the lens aperture is calculated taking into account that is generated by both the primary and the virtual source. Accordingly, the CST simulation now contains a small extension of a PPW filled with air after the lens aperture and "open add space" boundary condition. The normalized amplitude and phase distributions with and without dielectric loss are plotted in Fig. 7. The phase results of the RT and CST in Fig. 7(b) show good agreement, but some small discrepancies are found for the amplitude in Fig. 7(a). These deviations are mainly attributed to the fact that for simplicity, the effect of multiple reflections inside the lens is not considered in the RT model. However, small numerical errors in the amplitude of the electric field at the lens aperture have a minor effect on the far-field calculations, in contrast to the major influence that would have been observed if these small discrepancies were in terms of phase. This topic will be discussed in more detail later in Section III-B.

To better illustrate the ray tracing implemented with the proposed approach, some additional intermediate results are presented in Fig. 8 concerning the traced rays and the E-field distributions inside the lens at 30 GHz with the source f located at three different locations, $x = 0$, 1λ, and 2λ. A good collimation of the rays is clearly appreciated from the rays arriving parallel to the aperture. As shown in Fig. 8(a), when the lens antenna radiates in the broadside direction, the rays that exit the aperture are also well aligned, corresponding to the flat wavefront of the E-field in the lens aperture shown in Fig. 8(d). In the CST modeling, a flare with sinusoidal shape

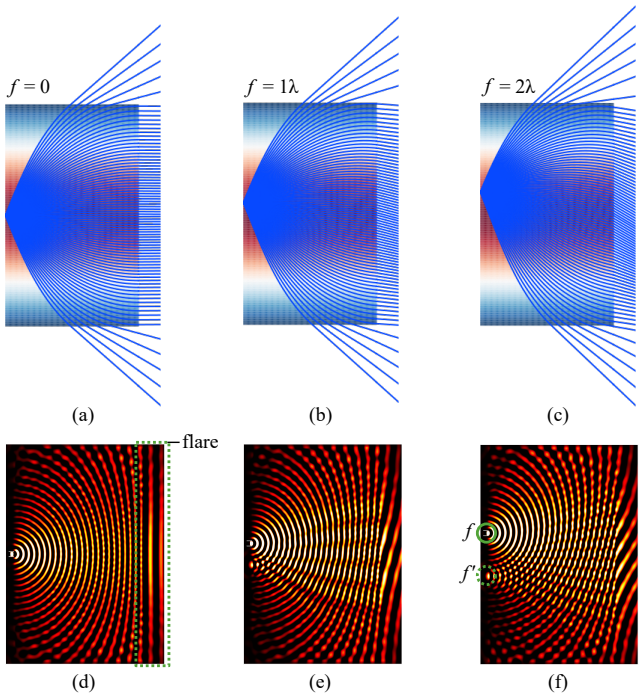

Fig. 8. (a)-(c): Ray tracing and (d)-(f) corresponding electric field distribution of the Mikaelian lens antenna at 30 GHz with the source f located at $x = 0$, 1λ, and 2λ.

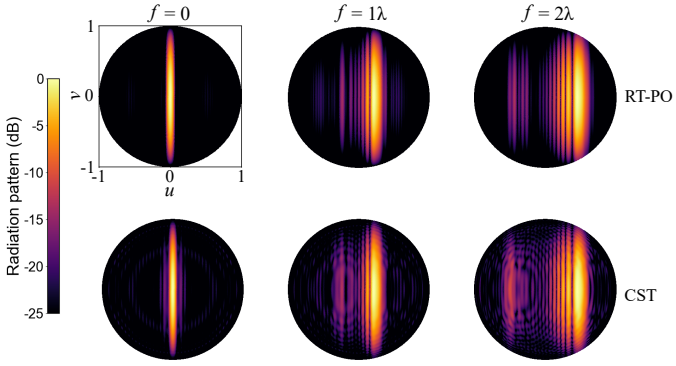

Fig. 9. Contour maps of the radiation patterns in the uv-plane at 30 GHz with the source f located at $x = 0$, 1λ, and 2λ obtained using RT-PO (upper row) and CST (lower row), under the same scale.

of 2 to 10 mm in height and a length of 18 mm is used to match the PPW Mikaelian lens with the free space, the same as in [52]. In the beam-scanning scenarios corresponding to the source f located at $x = 1\lambda$ and 2λ, Figs. 8(b)-(c) show that the rays are refracted non-parallel in the aperture due to the varying refractive index along the aperture characteristic of the Mikaelian lens. In accordance with the discussion in Sec. II-D, the reflected waves from the aperture shown in Figs. 8(e)-(f) (modeled as additional rays in the RT model, not explicitly shown in Figs. 8(b)-(c)) converge to a virtual source f' that reradiate out. Therefore, it is also clear that the total E-field distribution in the lens aperture is the superposition of the field from the primary and the virtual source, which applies to the total electric far field as well. An additional observation in Figs. 8(a)-(c) is that the rays that exit from the lateral sides

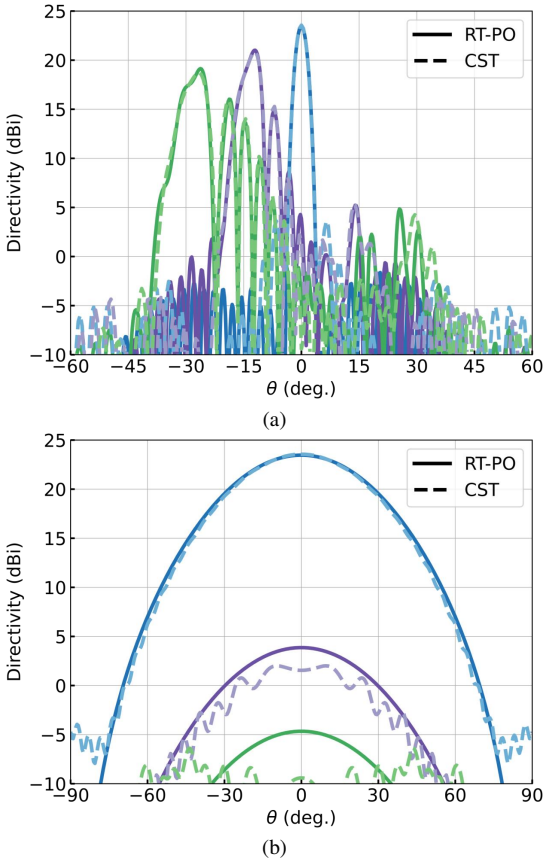

Fig. 10. Far-field directivity of the Mikaelian lens antenna at 30 GHz in the (a) H-plane ($\phi = 0$) and (b) E-plane ($\phi = \pi/2$) obtained by RT-PO (solid line) and CST full-wave simulation (dashed line) for the source f located at $x = 0$ (blue line), 1λ (purple line), and 2λ (green line).

of the lens explain the spillover effect, whose influence on the radiation characteristics will be shown in Section III-B.

B. Radiation Characteristics

Next, we present numerical results of the radiation characteristics obtained with the RT-PO model, which are compared to full-wave (CST) simulations, including radiation patterns in the uv-plane, principal E- and H-plane patterns, directivity, gain, and dielectric efficiencies. The contour maps of the radiation patterns in the uv-plane at 30 GHz with the source f located at $x = 0$, 1λ, and 2λ are reported in Fig. 9, where the upper and lower rows correspond to the results of the RT-PO model and the full-wave simulation of CST. It is apparent that the RT-PO model precisely predicts the main beam and the side lobes, whereas the ring-shaped side lobes caused by the diffraction effect in the edge of the lens flare shown in the full-wave simulations are not present in the RT-PO model. Note that the diffraction side lobes are well below the level of the main beam, as expected. In terms of computational effort, the RT-PO model performs in less than 5 s, while the CST model requires 16M cells and 30 min on a computer with a 64 bit operating system and 128 GB RAM.

Figure 10 shows the far-field directivity in the principal E- and H-planes, which gives a more detailed comparison between the results of the RT-PO model (solid line) and

the full-wave CST simulation (dashed line). The results in the H-plane ($\phi = 0$), which is the beamforming plane, are plotted in Fig. 10(a), where the blue, purple, and green lines represent the curves for the source f located at $x = 0$, 1λ, and 2λ, respectively. In this figure, the accuracy in agreement of the main beam from the RT-PO model and the CST results can be clearly appreciated. It is also apparent that the peak directivity values are well estimated, as well as the pattern shapes, including the side lobes in the opposite direction of the main beam, contributed by the virtual source. Finally, we can observe some additional lobes below 0 dBi caused by the spillover effect. Note that these low-level lobes in the CST results are more irregular because of the superposition of the spillover and diffraction effects.

The directivity data in the E-plane ($\phi = \pi/2$) are plotted in Fig. 10(b). Since the aperture width in the E-plane is only 10 mm, which is much smaller than the one in the H-plane, the beamwidths in Fig. 10(b) are much wider. When the source f is located at $x = 0$, the beam shape obtained using the RT-PO model and the CST simulation agree well with very small discrepancies. In beam-scanning scenarios, where the main beam is shifted away from the E-plane, the agreement worsens, with ripples in the CST results that are not present in the RT-PO predictions. As mentioned above, these ripples are mainly caused by diffraction effects; and since their level is around 20 dB lower than that of the main beam, they are negligible in most cases.

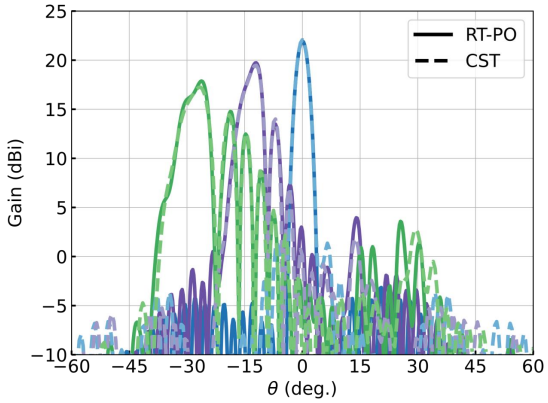

Fig. 11. Far-field gain of the Mikaelian lens antenna at 30 GHz in the H-plane ($\phi = 0$) obtained by RT-PO (solid line) and CST full-wave simulation (dashed line) for the source f located at $x = 0$ (blue line), 1λ (purple line), and 2λ (green line).

The RT-PO algorithm also allows for the computation of the far-field gain of the Mikaelian lens antenna considering dielectric losses, which can be further used to assess the dielectric efficiency. For brevity, only the results in the beamforming H-plane are shown in Fig. 11. Compared to the directivity results in Fig. 10(a), the gain patterns have a similar beam shape with a lower peak value due to dielectric losses. As a result, the corresponding dielectric efficiencies e_d are obtained and shown in Table I. The dielectric efficiencies obtained using the RT-PO model agree well with the CST results, with relatively larger discrepancies occurring in the beam-scanning cases. These discrepancies are due to the increased dielectric losses in multiple reflections, which are not taken into account in our model.

TABLE I
DIELECTRIC EFFICIENCIES OBTAINED WITH RT-PO AND CST

Model	$x = 0$	$x = 1\lambda$	$x = 2\lambda$
RT-PO	70.5%	74.5%	74.8%
CST	71.0%	71.5%	71.3%

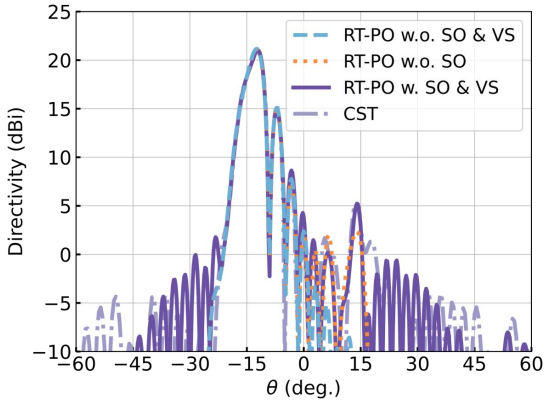

Fig. 12. Far-field directivity of the Mikaelian lens antenna at 30 GHz in the H-plane obtained by RT-PO with or without spillover or virtual source effect and CST full-wave simulation for the source f located at $x = 1\lambda$.

To examine the impact of spillover and virtual-source effects on RT-PO predictions, Fig. 12 compares the CST full-wave simulations when the source f is positioned at $x = 1\lambda$ with RT-PO results with and without the spillover (SO) or virtual-source (VS) effects. The findings reveal a notable correspondence between RT-PO results and CST simulations, even when disregarding the spillover and virtual-source effects, particularly on the main beam's shape and the main side lobes above 5 dBi. The presence of the virtual source is clearly evident in the orange-dotted curve, significantly impacting directivity at angles opposing the main beam direction, consequently giving rise to side lobes. The magnitude of these side lobes is determined by the refractive-index distribution across the lens aperture. Moreover, a comparison between the solid-purple curve and the orange-dotted curve suggests that the side lobes below 0 dBi can reasonably be attributed to the spillover effect. In conclusion, for a more accurate prediction of the radiation characteristics of the Mikaelian lens antenna, particularly under circumstances involving strong reflections within the lens aperture, the inclusion of both spillover and virtual-source effects within the RT-PO model is imperative.

IV. CONCLUSION

In this manuscript, we presented an accurate and efficient RT-PO approach for the analysis of planar Mikaelian lens antennas. This numerical method combines geometric and physical optics. Geometric optics is used to obtain the phase and amplitude information of the electric field in the lens aperture. Phase information is extracted from the rays that are traced from the feed to the lens aperture making use of Snell's law, whereas amplitude information is given by the ray-tube power conservation theory. The 3-D far-field pattern

radiated by the lens aperture is finally computed with the field equivalence principle, which is a PO approximation. Information on directivity, gain, and dielectric efficiency is obtained by considering a small dielectric loss of the lens. The unique characteristic of a virtual source for the Mikaelian lens and the spillover effect are further included in the RT-PO model. The 3-D far-zone electric fields evaluated with the proposed approach have been satisfactorily validated by comparison to the commercial full-wave simulator CST for a particular Mikaelian lens antenna. The RT-PO model provides a precise description of lens radiation characteristics with a computation time factor of approximately 300 times less than the CST model. This feature is particularly useful when the RT-PO model is exploited to design Mikaelian lens antennas or other PPW beamformers through optimization. Future work will explore the use of this RT-PO model applied to more general Mikaelian lens antennas to improve scanning performance and even other PPW lens antennas with arbitrary aperture shapes, such as geodesic lens antennas.

APPENDIX

A. Far-Zone E-fields for PPW Mikaelian Lenses

For the derivation of the far-zone E-field, we start with $\widetilde{L}_\theta$ and $\widetilde{L}_\phi$ in (15). For the specific aperture orientation shown in Fig. 4, where the aperture is in the xy-plane and the equivalent magnetic source only has the x-component, the $\widetilde{L}_\theta$ and $\widetilde{L}_\phi$ are found to be

$$\widetilde{L}_\theta = \cos\theta\cos\phi\frac{\sin Y}{Y}\widetilde{E}_a(k_0\sin\theta\cos\phi) \tag{27}$$

$$\widetilde{L}_\phi = -\sin\phi\frac{\sin Y}{Y}\widetilde{E}_a(k_0\sin\theta\cos\phi) \tag{28}$$

where a and b are the length and width of the lens aperture respectively, $\mathbf{k}_0\cdot\mathbf{r}'$ is equal to $k_0(x'\sin\theta\cos\phi+y'\sin\theta\sin\phi)$, $Y=(k_0b/2)\sin\theta\sin\phi$, and $\widetilde{E}_a(q)$ is the Fourier transform of $E_a(x)$. Although this Fourier transform can be numerically computed in different efficient ways, here we propose to apply a simple Simpson rule using the obtained E-field distribution of the traced rays in (11). As a result, the field radiated by the lens aperture can finally be calculated as ($E_r=0$)

$$E_\theta(\theta,\phi) = \mathrm{j}k_0b\frac{\mathrm{e}^{-\mathrm{j}k_0r}}{2\pi r}\sin\phi\frac{\sin Y}{Y} \times\sum_k A_k\mathrm{e}^{-\xi_k}\mathrm{e}^{-\mathrm{j}(\Phi_k-k_0x_k\sin\theta\cos\phi)}\delta L_k \tag{29}$$

$$E_\phi(\theta,\phi) = \mathrm{j}k_0b\frac{\mathrm{e}^{-\mathrm{j}k_0r}}{2\pi r}\cos\theta\cos\phi\frac{\sin Y}{Y} \times\sum_k A_k\mathrm{e}^{-\xi_k}\mathrm{e}^{-\mathrm{j}(\Phi_k-k_0x_k\sin\theta\cos\phi)}\delta L_k\ . \tag{30}$$

B. Derivation of Directivity and Gain

For the derivation of directivity, the average radiated power density P_{rad} is first formed using the fields in the lens aperture and then integrated over the whole aperture bounded by the surrounding PEC. We assume that the magnetic field in the aperture is given by $\mathbf{H}_a = -(E_a/\eta_a)\hat{\mathbf{x}}$ where the wave impedance in the aperture is given by $\eta_a=\eta_0/(\hat{\mathbf{s}}_k\cdot\hat{\mathbf{n}}_k)$, with η_0 being the free-space wave impedance. After some simple derivations, the directivity and gain can be obtained as

$$D(\theta,\phi)=\frac{4\pi U}{P_{\text{rad}}}\approx\frac{4\pi r^2\left(|E_\theta|^2+|E_\phi|^2\right)}{b\sum_k A_k^2\,\mathrm{e}^{-2\xi_k}(\hat{\mathbf{s}}_k\cdot\hat{\mathbf{n}}_k)\delta L_k} \tag{31}$$

$$G(\theta,\phi)=\frac{4\pi U}{P_{\text{in}}}\approx\frac{4\pi r^2\left(|E_\theta|^2+|E_\phi|^2\right)}{b\sum_k A_k^2(\hat{\mathbf{s}}_k\cdot\hat{\mathbf{n}}_k)\delta L_k}\ . \tag{32}$$

REFERENCES

[1] M. Elkashlan, T. Q. Duong, and H.-H. Chen, "Millimeter-wave communications for 5G: fundamentals: Part I [Guest Editorial]," *IEEE Commun. Mag.*, vol. 52, no. 9, pp. 52–54, Sep. 2014.

[2] M. Elkashlan, T. Q. Duong, and H.-h. Chen, "Millimeter-wave communications for 5G – Part 2: applications [Guest Editorial]," *IEEE Commun. Mag.*, vol. 53, no. 1, pp. 166–167, Jan. 2015.

[3] P. S. Hall and S. J. Vetterlein, "Review of radio frequency beamforming techniques for scanned and multiple beam antennas," *IEE Proc. H-Microw. Antennas Propag.*, vol. 137, pp. 293–303, Oct. 1990.

[4] O. Quevedo-Teruel, M. Ebrahimpouri, and F. Ghasemifard, "Lens antennas for 5G communications systems," *IEEE Comm. Mag.*, vol. 56, no. 7, pp. 36–41, Jul. 2018.

[5] Y. J. Guo, M. Ansari, R. W. Ziolkowski, and N. J. G. Fonseca, "Quasi-optical multi-beam antenna technologies for B5G and 6G mmWave and THz networks: a review," *IEEE Open J. of Antennas Propag.*, vol. 2, pp. 807–830, Jun. 2021.

[6] W. Rotman, "Wide-angle scanning with microwave double-layer pillboxes," *IRE Trans. Antennas Propag.*, vol. 6, no. 1, pp. 96–105, Jan. 1958.

[7] M. Ettorre, R. Sauleau, and L. Le Coq, "Multi-beam multi-layer leaky-wave SIW pillbox antenna for millimeter-wave applications," *IEEE Trans. Antennas Propag.*, vol. 59, no. 4, pp. 1093–1100, Apr. 2011.

[8] D. Filipovic, S. Gearhart, and G. Rebeiz, "Double-slot antennas on extended hemispherical and elliptical silicon dielectric lenses," *IEEE Trans. Microw. Theory Tech.*, vol. 41, no. 10, pp. 1738–1749, Oct. 1993.

[9] G. Godi, R. Sauleau, and D. Thouroude, "Performance of reduced size substrate lens antennas for millimeter-wave communications," *IEEE Trans. Antennas Propag.*, vol. 53, no. 4, pp. 1278–1286, Apr. 2005.

[10] N. Llombart, G. Chattopadhyay, A. Skalare, and I. Mehdi, "Novel Terahertz antenna based on a silicon lens fed by a leaky wave enhanced waveguide," *IEEE Trans. Antennas Propag.*, vol. 59, no. 6, pp. 2160–2168, Jun. 2011.

[11] H. F. Ma, B. G. Cai, T. X. Zhang, Y. Yang, W. X. Jiang, and T. J. Cui, "Three-dimensional gradient-index materials and their applications in microwave lens antennas," *IEEE Trans. Antennas Propag.*, vol. 61, no. 5, pp. 2561–2569, May 2013.

[12] H.-X. Xu, G.-M. Wang, Z. Tao, and T. Cai, "An octave-bandwidth half Maxwell fish-eye lens antenna using three-dimensional gradient-index fractal metamaterials," *IEEE Trans. Antennas Propag.*, vol. 62, no. 9, pp. 4823–4828, Sep. 2014.

[13] O. Quevedo-Teruel, Q. Liao, Q. Chen, P. Castillo-Tapia, F. Mesa, K. Zhao, and N. J. G. Fonseca, "Geodesic lens antennas for 5G and beyond," *IEEE Commun. Mag.*, vol. 60, no. 1, pp. 40–45, 2022.

[14] T. Ströber, S. Tubau, E. Girard, H. Legay, G. Goussetis, and M. Ettorre, "Shaped parallel-plate lens for mechanical wide-angle beam steering," *IEEE Trans. Antennas Propag.*, vol. 69, no. 12, pp. 8158–8169, Dec. 2021.

[15] R. K. Luneburg, *Mathematical Theory of Optics*. Berkeley, CA, USA: Univ. California Press, 1944.

[16] B. Fuchs, O. Lafond, S. Rondineau, and M. Himdi, "Design and characterization of half Maxwell fish-eye lens antennas in millimeter waves," *IEEE Trans. Microw. Theory Tech.*, vol. 54, no. 6, pp. 2292–2300, Jun. 2006.

[17] Z. L. Mei, J. Bai, T. M. Niu, and T. J. Cui, "A half Maxwell fish-eye lens antenna based on gradient-index metamaterials," *IEEE Trans. Antennas Propag.*, vol. 60, no. 1, pp. 398–401, Jan. 2012.

[18] A. S. Gutman, "Modified Luneburg lens," *J. Appl. Phys.*, vol. 25, no. 7, pp. 855–859, Jul. 1954.

[19] O. Zetterstrom, N. J. G. Fonseca, and O. Quevedo-Teruel, "Additively manufactured half-Gutman lens antenna for mobile satellite communications," *IEEE Antennas Wirel. Propag. Lett.*, vol. 22, no. 4, pp. 759–763, Apr. 2023.

[20] U. Leonhardt, "Optical conformal mapping," *Science*, vol. 312, no. 5781, pp. 1777–1780, Jun. 2006.
[21] J. Li and J. B. Pendry, "Hiding under the carpet: a new strategy for cloaking," *Phys. Rev. Lett.*, vol. 101, no. 20, p. 203901, Nov. 2008.
[22] H. F. Ma and T. J. Cui, "Three-dimensional broadband and broad-angle transformation-optics lens," *Nat. Commun.*, vol. 1, no. 1, p. 124, Nov. 2010.
[23] M. Ebrahimpouri and O. Quevedo-Teruel, "Bespoke lenses based on quasi-conformal transformation optics technique," *IEEE Trans. Antennas Propag.*, vol. 65, no. 5, pp. 2256–2264, 2017.
[24] A. L. Mikaelian, "Using of layered media for focusing waves," *Dokladi Academii Nauk SSSR*, vol. 81, no. N4, p. 569, 1951.
[25] A. L. Mikaelian and A. M. Prokhorov, "Self-focusing media with variable index of refraction," *Progress in Optics*, vol. 17, pp. 279–345, 1980.
[26] J. Bor, B. Fuchs, O. Lafond, and M. Himdi, "Flat foam-based Mikaelian lens antenna for millimeter wave applications," in *2014 11th European Radar Conference*, pp. 337–340, Dec. 2014.
[27] J. W. Yang, W. Y. Lai, H. C. Chou, and M. N. M. Kehn, "Compact Mikaelian lens synthesized by metasurfaces," *IEEE Antennas Wirel. Propag. Lett.*, vol. 17, no. 3, pp. 397–400, Mar. 2018.
[28] Z. Zhang, Y. Tong, Y. Wang, and H. K. Tsang, "Nonparaxial mode-size converter using an ultracompact metamaterial Mikaelian lens," *J. Light. Technol.*, vol. 39, no. 7, pp. 2077–2083, Apr. 2021.
[29] J. Chen, H. C. Chu, Y. Lai, Z. Liu, H. Chen, M. Chen, and D. Fang, "Conformally mapped Mikaelian lens for broadband achromatic high resolution focusing," *Laser Photonics Rev.*, vol. 15, no. 5, p. 2000564, May. 2021.
[30] W. Shao and Q. Chen, "Performance analysis of an all-dielectric planar Mikaelian lens antenna for 1-D beam-steering application," *Opt. Express*, vol. 29, no. 18, pp. 29202–29214, Aug. 2021.
[31] W. Shao and Q. Chen, "2-D beam-steerable generalized Mikaelian lens with unique flat-shape characteristic," *IEEE Antennas Wirel. Propag. Lett.*, vol. 20, no. 10, pp. 2033–2037, Oct. 2021.
[32] R. F. Rinehart, "A family of designs for rapid scanning radar antennas," *Proc. IRE*, vol. 40, no. 6, pp. 686–688, Jun. 1952.
[33] K. S. Kunz, "Propagation of microwaves between a parallel pair of doubly curved conducting surfaces," *J. Appl. Phys.*, vol. 25, no. 5, pp. 642–653, May 1954.
[34] R. Mitchell-Thomas, O. Quevedo-Teruel, T. McManus, S. Horsley, and Y. Hao, "Lenses on curved surfaces," *Opt. Lett.*, vol. 39, no. 12, pp. 3551–3554, Jun. 2014.
[35] O. Quevedo-Teruel, J. Miao, M. Mattsson, A. Algaba-Brazalez, M. Johansson, and L. Manholm, "Glide-symmetric fully metallic Luneburg lens for 5G communications at Ka-band," *IEEE Antennas Wirel. Propag. Lett.*, vol. 17, no. 9, pp. 1588–1592, Sep. 2018.
[36] Q. Liao, N. J. G. Fonseca, and O. Quevedo-Teruel, "Compact multibeam fully metallic geodesic Luneburg lens antenna based on non-Euclidean transformation optics," *IEEE Trans. Antennas Propag.*, vol. 66, no. 12, pp. 7383–7388, Dec. 2018.
[37] Q. Liao, N. J. G. Fonseca, M. Camacho, A. Palomares-Caballero, F. Mesa, and O. Quevedo-Teruel, "Ray-tracing model for generalized geodesic lens multiple beam antennas," *IEEE Trans. Antennas Propag.*, vol. 71, no. 3, pp. 2640–2651, Mar. 2023.
[38] N. J. G. Fonseca, Q. Liao, and O. Quevedo-Teruel, "Equivalent planar lens ray-tracing model to design modulated geodesic lenses using non-Euclidean transformation optics," *IEEE Trans. Antennas Propag.*, vol. 68, no. 5, pp. 3410–3422, May 2020.
[39] Q. Chen, S. A. R. Horsley, N. J. G. Fonseca, T. Tyc, and O. Quevedo-Teruel, "Double-layer geodesic and gradient-index lenses," *Nat. Commun.*, vol. 13, no. 1, pp. 1–12, Apr. 2022.
[40] F. Doucet, N. J. G. Fonseca, E. Girard, H. Legay, and R. Sauleau, "Analytical model and study of continuous parallel plate waveguide lens-like multiple-beam antennas," *IEEE Trans. Antennas Propag.*, vol. 66, no. 9, pp. 4426–4436, Sep. 2018.
[41] F. Doucet, N. J. G. Fonseca, E. Girard, X. Morvan, L. Le Coq, H. Legay, and R. Sauleau, "Shaped continuous parallel plate delay lens with enhanced scanning performance," *IEEE Trans. Antennas Propag.*, vol. 67, no. 11, pp. 6695–6704, Nov. 2019.
[42] T. Ströber, S. Tubau, E. Girard, H. Legay, G. Goussetis, and M. Ettorre, "Shaped parallel-plate lens for mechanical wide-angle beam steering," *IEEE Trans. Antennas Propag.*, vol. 69, no. 12, pp. 8158–8169, Dec. 2021.
[43] F. Doucet, N. J. G. Fonseca, E. Girard, X. Morvan, and R. Sauleau, "Compact planar beamformer using multiple continuous parallel-plate waveguide delay lenses," *IEEE Antennas Wirel. Propag. Lett.*, vol. 21, no. 11, pp. 2229–2233, Nov. 2022.
[44] W. Wang and J. Chisum, "Hybrid geometrical optics and uniform asymptotic physical optics for rapid and accurate practical GRIN lens design," in *IEEE MTT-S Int. Microw. Symp. Digest*, pp. 20–23, 2022.
[45] S. Silver, *Microwave antenna theory and design*. IET, 1984.
[46] Y. A. Kravtsov and Y. I. Orlov, *Geometrical Optics of Inhomogeneous Media*, vol. 38. Springer, 1990.
[47] M. Born, E. Wolf, and A. Bhatia, *Principles of Optics: Electromagnetic Theory of Propagation, Interference and Diffraction of Light*. Cambridge University Press, 1999.
[48] C. A. Balanis, *Antenna theory: analysis and design*. John Wiley & Sons, 2016.
[49] S. Orfanidis, *Electromagnetic Waves and Antennas* [Online]. Available: https://www.ece.rutgers.edu/ orfanidi/ewa/., 2016.
[50] S. Yang, Q. Chen, F. Mesa, N. J. G. Fonseca, and O. Quevedo-Teruel, "Geodesic half-Maxwell fish-eye lens antenna," *IEEE Trans. Antennas Propag.*, vol. 71, no. 3, pp. 2330–2338, Mar. 2023.
[51] O. Zetterstrom, P. Arnberg, F. V. Vidarsson, A. Algaba-Brazález, L. Manholm, M. Johansson, and O. Quevedo-Teruel, "V-band geodesic generalized Luneburg lens antenna with high beam crossover gain," *IEEE Trans. Antennas Propag.*, vol. 71, no. 9, pp. 7591–7596, Sep. 2023.
[52] M. Chen, F. Mesa, and O. Quevedo-Teruel, "Geodesic H-plane horn antennas," *IEEE Trans. Antennas Propag.*, vol. 71, no. 8, pp. 6329–6339, Aug. 2023.

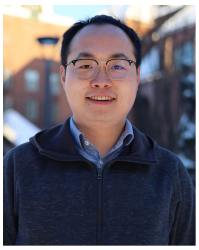

Mingzheng Chen (Student Member, IEEE) received the B.Sc. and M.Sc. from Southeast University, Nanjing, China, in 2018 and 2021, respectively. Since 2021, he has pursued his Ph.D. degree with the Division of Electromagnetic Engineering and Fusion Science in the School of Electrical Engineering and Computer Science at KTH Royal Institute of Technology in Stockholm, Sweden. His current research interest includes ray tracing, physical optics, and lens antennas.

Ozum Habiboglu His biography is not available at this moment.

Francisco Mesa (Fellow, IEEE) received the Licenciado and Ph.D. degrees in physics from the Universidad de Sevilla, Seville, Spain, in 1989 and 1991, respectively. He is currently a Professor with the Departamento de Física Aplicada 1, Universidad de Sevilla. His research interest includes electromagnetic propagation/radiation in microwave and quasi-optical structures.

O. Quevedo-Teruel (Fellow, IEEE) received his Telecommunication Engineering and Ph.D. Degrees from Carlos III University of Madrid, Spain in 2005 and 2010. From 2010-2011, Oscar Quevedo-Teruel joined the Department of Theoretical Physics of Condensed Matter at Universidad Autonoma de Madrid as a research fellow and went on to continue his postdoctoral research at Queen Mary University of London from 2011-2013.

In 2014, he joined KTH Royal Institute of Technology in Stockholm, Sweden where he is a Professor and Director of the Master Programme in Electromagnetics Fusion and Space Engineering. He has been an Associate Editor of the IEEE Transactions on Antennas and Propagation from 2018-2022 and Track Editor since 2022. He is also the founder and editor-in-chief of the EurAAP journal Reviews of Electromagnetics since 2020. He was the EurAAP delegate for Sweden, Norway, and Iceland from 2018-2020 and he has been a member of the EurAAP Board of Directors since January 2021. Since January 2022, he is the vice-chair of EurAAP. He was a distinguished lecturer of the IEEE Antennas and Propagation Society for the period 2019-2021. He is the Chair of the IEEE APS Educational Initiatives Programme since 2020.

He has made scientific contributions to higher symmetries, transformation optics, lens antennas, metasurfaces, and high-impedance surfaces. He is the co-author of more than 140 papers in international journals and 250 at international conferences.